Journal of Applied Physics

Metal-carbon nanotube composite for wavelength-selective bolometer with improved characteristics

Cite as: J. Appl. Phys. **133**, 043104 (2023); https://doi.org/10.1063/5.0129993
Submitted: 08 October 2022 • Accepted: 02 January 2023 • Published Online: 24 January 2023

Sukanta Nandi, Vinod Panwar and Abha Misra

Journal of Applied Physics ARTICLE scitation.org/journal/jap

Metal-carbon nanotube composite for wavelength-selective bolometer with improved characteristics

Cite as: J. Appl. Phys. **133**, 043104 (2023); doi: 10.1063/5.0129993
Submitted: 8 October 2022 · Accepted: 2 January 2023 ·
Published Online: 24 January 2023

Sukanta Nandi, Vinod Panwar, and Abha Misra[a)]

AFFILIATIONS

Department of Instrumentation and Applied Physics, Indian Institute of Science, Bangalore, Karnataka 560012, India

[a)]**Author to whom correspondence should be addressed:** abha.misra1@gmail.com

ABSTRACT

This work comprehensively discusses the utilization of a metal-multiwalled carbon nanotube (CNT) nanocomposite of gold (Au)/CNT for uncooled bolometric application synthesized by a simple rapid green synthesis technique. Enhanced light–matter interaction with the visible (532 nm) and near-infrared (1064 nm) radiations in the nanocomposite is utilized for achieving improved bolometric response at room temperature (RT, ∼300 K). A comparatively higher temperature coefficient of resistance of ∼−0.11%/K (improvement of ∼57%) was achieved in the Au/CNT nanocomposite bolometer (BM). Additionally, the composite BM demonstrated a dual (532 and 1064 nm) spectral selectively and enhanced sensitivity with respective large RT voltage responsivities of ∼11.70 ± 3.45 V/W and ∼503.54 ± 12.77 mV/W, as opposed to null response from the CNT BM. The current study, thus, demonstrates an important step toward designing high-performing CNT BMs for uncooled operation, with added functionality of wavelength-selectiveness.

I. INTRODUCTION

The multiwall carbon nanotube (CNT) is one of the promising bolometric materials due to its broadband optical absorption, high infrared (IR) absorption, naturally suspended concentric tubes, and electrically conductive and intrinsic one-dimensional nature.[1–5] Apart from being a good bolometric material, these multiwalled nanotubes possess high surface-to-volume ratio, altogether with a strong resilience toward thermal/mechanical stresses and chemical treatments.[6–12] Additionally, their large strength-to-weight ratio is an added value for the formation of freestanding films, an extremely important parameter in bolometer (BM) technology.[1,3,13] From the viewpoint of practical implementation, these nanotubes are compatible with silicon (Si) microfabrication technology and have also displayed strong promises toward a disruptive technology.[14–16] All these exceptional properties offer its prospects for future device applications.[17] Though being an ideal bolometric material, the performance of the CNT-based BM can be further improved via various surface treatment methodologies. These include thermal annealing of the CNT film,[1,18] functionalization with various molecules and radicals,[4] surface modification with other nanoparticles (NPs),[3,19,20] forming hybrids with other NPs,[21,22] etc. One of the ways to achieve this is to surface functionalize the CNT with metal NPs.[23] Surface modification with metal NPs lead to confinement of photonic heat at the hybrid junction owing to involved plasmonic and photothermal effects. The primary advantage of such a confinement is improved nanoscale light–matter interaction. The plasmonic effect arises from collective oscillation of the electron cloud (plasmon) upon incidence of an electromagnetic radiation on the metal NPs (wavelength much larger than the NP size).[24,25] These generated localized surface plasmons result in the electric field confinement that, in turn, results in increased localized heating.[26] This effect has been utilized by various researchers in improving the IR detection properties of nanotubes via structurally engineered schemes.[26–28] Next, the choice of the metal plasmonic material is also a matter of extreme importance from the view-point of stability and application. Among the various metal NPs, like silver (Ag), gold (Au), aluminum, copper, palladium, platinum, and alkali metals, Au is a promising plasmonic material due to its excellent performance in the visible and near IR, together with high stability under ambient conditions.[29] Au, on the other hand, when coupled with carbon nanotubes, has resulted in improved sensing and photodetection. The improved device performance arises from the synergistic effect

of the Au/carbon nanotube coupled system.[30–34] Nevertheless, the room temperature (~300 K, RT), i.e., uncooled, bolometric properties of the Au/CNT system in the form of a nanocomposite remain unexplored.

Toward photodetection, different approaches, however, have been adapted by several groups to work on plasmonic-based CNT photodetectors (PDs). Plasmonic PDs are optical detectors that incorporate metallic or plasmonic materials/structures together with the active photodetection element. The general role of plasmonic elements in these PDs is to either generate hot-carriers or confine light and thereby result in improved photodetection.[35–39] Apart from metals (which have high concentration of free electrons), metallic alloys such as noble-transition alloys, alkali-noble inter-metallic compounds, heavily doped semiconductors (e.g., aluminum-doped zinc oxide), etc., have turned out to be alternative candidates for plasmonic materials.[40–42] A metal-dielectric interface or an interface, where a change in sign of the dielectric function real component (of the materials) is observed, is required to host these surface plasmons.[29,43] Additionally, a wide range of parameters, such as NP/nanostructure (NS) shape, size, optical properties of the surrounding environment/host material, carrier mobility, etc., greatly affect the plasmonic properties of these systems.[42,44] For instance, Zhou *et al.* reported a three times photocurrent enhancement in ultralong single-walled carbon nanotubes (SWCNT) coupled with Au NPs for 632.8 nm wavelength.[34] The PD was fabricated by stamping dodecanethiol-capped Au NPs using a polydimethylsiloxane slab on top of chemical vapor deposition (CVD)-grown SWCNT. Upon light illumination, strong local field enhancement resulting from coupling with Au NPs led to the enhanced photocurrent. In another report by Liu *et al.*, visible light detection was achieved using a device of SWCNT covered partly with Au NSs.[45] The device was fabricated by dropcasting the Au NSs (NPs and nanorods), synthesized via a chemical route, on one section of the SWCNT film leaving the other side pristine. The phenomenon of surface plasmon resonance (SPR) of the Au NSs was used to create a temperature difference between the two regions of the film resulting in an open circuit voltage. Additionally, Samani *et al.* demonstrated plasmonic-enhanced RT CNT IR BM with high voltage responsivity (R_v) and improved temperature coefficient of resistance (TCR).[26] The BM in the form of a nanoantenna-CNT array was, however, fabricated employing complex time-consuming nanofabrication techniques of electron beam lithography and a laser-assisted CVD. Furthermore, the nanoantennas were of Ag, which are highly prone to oxidation with time.

The current work, thus, focuses on overcoming these challenges by reporting a simple rapid green synthesis of Au/CNT nanocomposite (AuC) for RT (uncooled) bolometric application. The nanocomposite BM displays an enhanced bolometric response together with wavelength selectiveness as an added functionality. A maximum RT TCR of ~−0.11%/K is obtained for the BM with an average R_v of ~503.54 ± 12.77 mV/W and ~11.70 ± 3.45 V/W, respectively, for the IR and visible wavelengths.

II. RESULTS AND DISCUSSIONS

A. Material synthesis and characterization

The green synthesis method was adopted for *in situ* functionalization of CNT with Au NPs. CNT was synthesized using CVD and then purified to remove amorphous carbon (C) and metal catalyst impurities; details of growth and purification are provided in previous works.[3,19] *In situ* surface functionalization of CNT with the Au NPs was then carried out by adding as-prepared CNT into a solution of $HAuCl_4$.$3H_2O$ and then adding the *Mangifera indica* leaf extract, which acts both as a green reducing as well as the capping agent. The procedure for obtaining the extract can be found in the literature.[46] Initially, ~0.031 g of $HAuCl_4$.$3H_2O$ was added in 100 ml of de-ionized (DI) water to prepare a stock solution. From the stock solution, 20 ml of solution was isolated in a vial to which 2.5 ml of the extract was added along with 2 mg/ml of CNT, and the sample is named as AuC. *In situ* functionalized CNT with Au NPs were then dried to evaporate the water and then ultrasonicated with *N*,*N*-dimethylmethanamide (DMF). For device fabrication, 75 ml of the uniform dispersion in DMF was then spray coated to form a thin film of the bolometric material. The fabricated films were then transferred between the two chromium/Au electrodes separated by ~4 μm. The electrodes were fabricated by the standard photolithography technique. The adopted methodology of device fabrication can be found in our previous report.[3]

Microstructures [scanning electron microscope (SEM) image] of purified CNT and Au functionalized CNT (AuC) are depicted in Figs. 1(a) and 1(b). Bottom right inset of Fig. 1(b) presents the high magnification transmission electron microscope (TEM) image of AuC, showing the attachment of Au NPs on the CNT surface. The CNTs are multiwalled, with diameter in the range of ~30–70 nm and of varying lengths, with maximum of ~1 mm. Next, from the low magnification TEM images, it is observed that Au NPs are distributed over the CNT surface as single particles and clusters, with average sizes of ~10–50 nm (Fig. S1 in the supplementary material). Furthermore, the energy-dispersive spectroscopy (EDS) spectrum of AuC (Fig. S2 in the supplementary material) reveals the presence of only C and Au in the nanocomposite, with impurities of oxygen (O) and Si. These impurities owing their origin from the underlying substrate (SiO_2/Si), that being used during the measurement.

Figure 1(c) presents the Raman spectra of CNT and AuC in the range of 1000–2000 cm^{-1}. Raman spectrum of the CNT depicts peaks at ~1342, ~1574, and ~1612.5 cm^{-1}. The peak at ~1342 cm^{-1} is assigned as D-band, i.e., defect-induced A_{1g} mode, originating from the out-of-plane vibration of disordered amorphous C and other structural defects. The second dominant peak at ~1574 cm^{-1} is known as G-band, which is the E_{2g} mode. This mode is a measure of graphitization extent in CNT and arises from the in-plane tangential vibration of the sp^2-bonded C atoms in the graphite lattice. Finally, the band at ~1612.5 cm^{-1} (D′) results from vibrational wave confinement arising from atomic displacement along the CNT circumference.[47,48] On the other hand, in the case of AuC, blue-shift of ~6 cm^{-1} is observed for both the D and G bands. The observed blue-shift is due to the interaction of Au NPs with the CNT that results in a shift in the electronic states and, thus, in Fermi energy.[47] Furthermore, I_D/I_G ratio for AuC is ~0.92 (~1.52 times higher than CNT). A comparatively higher value of the ratio in AuC is indicative of increased disorder compared to that of CNT. Another important observation is peak broadening (full width at half maximum, i.e., FWHM) of both D as well as G bands. The D and G bands in AuC, respectively, get widen by the factors of ~3.6 and ~2.9. Such a broadening is indicative of the

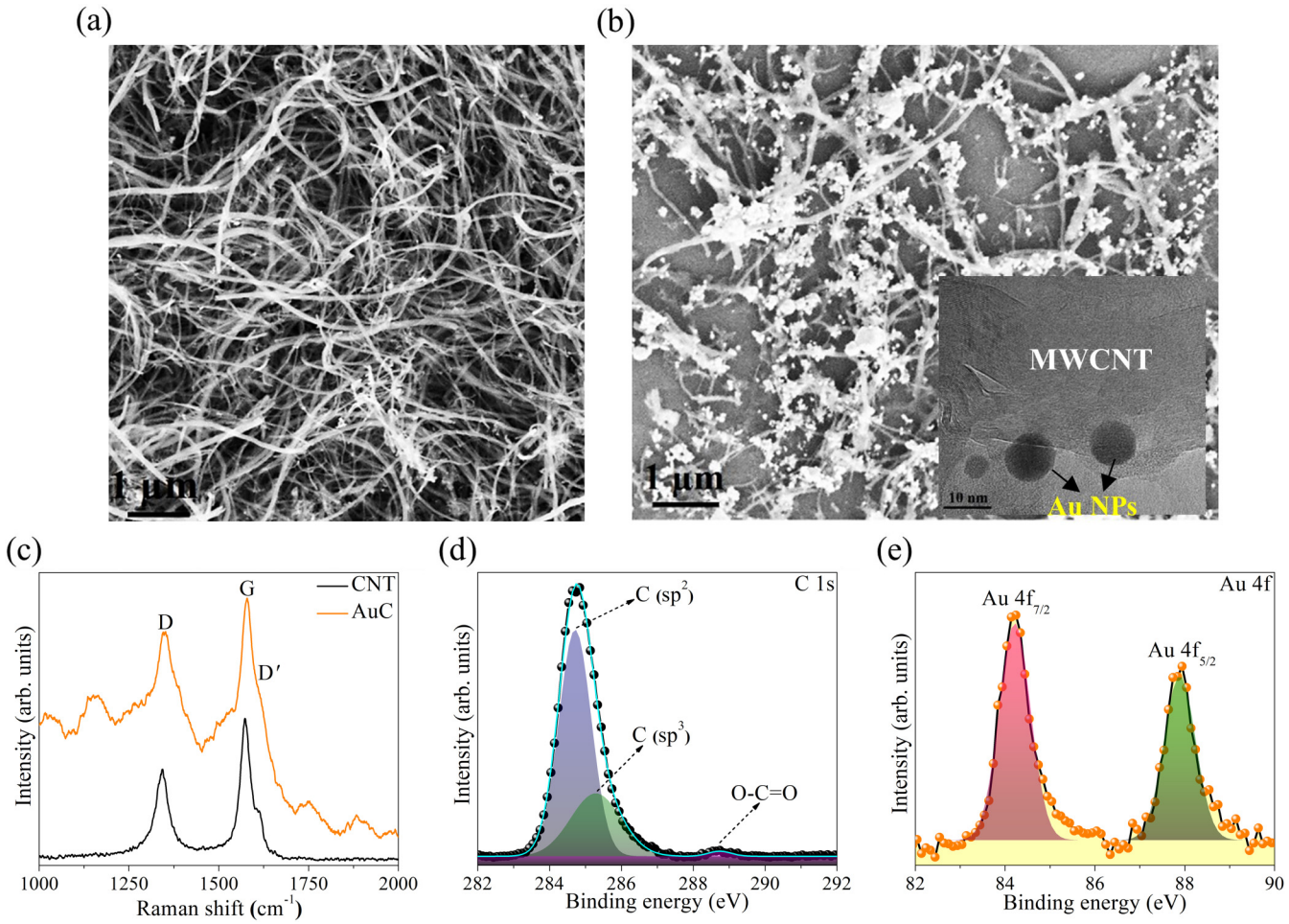

FIG. 1. SEM image of (a) CNT and (b) AuC with high magnification TEM image (bottom right inset). (c) Raman spectra of CNT and AuC. Deconvoluted XPS spectra of AuC for (d) C 1*s* and (e) Au 4*f*.

presence of charged impurities in AuC attributed by Au NPs.[49] Electronic states of C and Au in AuC were then investigated using x-ray photoelectron spectroscopy (XPS) spectra, as depicted in Figs. 1(d) and 1(e). Figure 1(d) presents the deconvoluted C 1*s* spectrum consisting of three distinct fitted peaks at ~284.7 (sp^2), ~285.3 (sp^3), and ~288.7 eV, attributed, respectively, to the species of the graphitic structure, structural defects, and moieties of C atoms attached to O molecules (O—C═O).[50–52] The core-level XPS spectrum of Au 4*f* is depicted in Fig. 1(e), where two distinct spin–orbit doublets are observed at ~84.2 and ~87.9 eV, respectively, to Au $4f_{7/2}$ and Au $4f_{5/2}$ of the metallic Au state (0 oxidation state).[50] Moreover, the absence of any peak around ~92 eV implies almost complete reduction in $AuCl_4^-$ (+3 oxidation state) into the metallic state [Fig. S3(a) in the supplementary material].[50] Furthermore, x-ray diffraction spectra of CNT and AuC are depicted in Fig. S3(b) in the supplementary material with diffraction peaks of CNT being observed at $2\Theta = \sim 26.25°$, ~43°, ~54°, and ~78° that correspond, respectively, to (002), (100), (004), and (110) diffraction planes of the graphitic structure.[3,19,53] The diffraction peaks in AuC are observed at $2\Theta = \sim 38.52°$, 44.60°, 64.76°, and 77.67°, which correspond to (111), (200), (220), and (311) planes of Au NPs, respectively, with the dominant (111) plane.[46,54,55]

B. Bolometric performance

The as-fabricated BM schematic is depicted in Fig. 2(a), with the micro-scale view (SEM) in Fig. S4 in the supplementary material, that has been analyzed for the bolometric response in the temperature range of 12–300 K. Figure 2(b) depicts the characteristic current–voltage (*I*–*V*) relationship of the AuC device along with the temperature variation. TCR of the BM, defined as, TCR $= \frac{\partial \ln R}{\partial T}$, where "*R*" is the resistance and "*T*" is the temperature, is further plotted against temperature in Fig. 2(c).

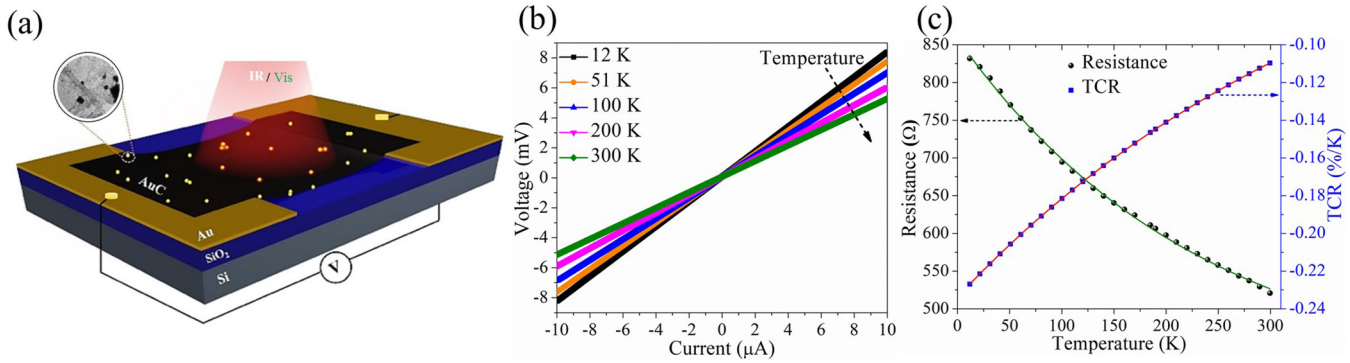

FIG. 2. (a) BM schematic and (b) temperature-dependent *I–V* characteristics of AuC BM. (c) The corresponding variation of resistance and TCR with temperature (continuous lines representing fitted curves).

The obtained *I-V* [Fig. 2(b)] were linear in nature, an indicative of ohmic contact of AuC with metal contacts. The device follows the same linear behavior throughout the temperature range of 12–300 K. Furthermore, it is observed from the *I-V* that with the increase in temperature, the voltage decreases for a fixed current, thus indicating a decrease in resistance with temperature (i.e., semiconducting behavior). Extracted resistance values are then plotted in Fig. 2(c), which varies as $\sim e^{-constant^{*}T}$. TCR, on the other hand, is extracted from the temperature-dependent slope of the "*R*" vs "*T*" curve and, thus, varies as $\sim -e^{-constant^{*}T}$, with values ranging from ∼−0.23 to −0.11%/K in the temperature range of 12–300 K. Obtained RT absolute TCR of the AuC BM (0.11%/K) is higher than that reported for CNT (0.06, 0.07, 0.08, 0.086, and 0.088%/K),[1,56–58] SWCNT (0.03, 0.07%/K),[18] CNT/graphene hybrid (0.08%/K),[59] and CNT–MoS_2 composite (∼0.075%/K)[21] BMs. Thus, an improvement in the range of ∼25%–267% was observed in the RT TCR value of the as-fabricated AuC BM.

1. Infrared bolometric characteristics

BMs of CNT and AuC were then characterized for their bolometric photoresponse (PR, $\Delta R/R_0$, $\Delta R =$ resistance during light ON–resistance during light OFF and R_0 is the resistance during light OFF, i.e., dark resistance) with 532 and 1064 nm wavelengths. The wavelengths were chosen based on the visible and NIR sensitivity of Au,[44,46,54,55,60–63] along with the 1064 nm bolometric sensitivity of CNT,[3,21] as reported previously.

Figure 3 compares the variation in IR induced (1064 nm) PR and R_v with varying incident illumination power (P_{inc}, normalized with the device active area)[3] in the range of ∼0.11–0.41 mW for both CNT and AuC BMs at RT. The corresponding photovoltage (voltage difference between IR and dark, ΔV) is presented in Fig. S5(a) in the supplementary material. It is observed, respectively, from Fig. 3(a) and Fig. S5(a) in the supplementary material that both the PR as well as ΔV of the AuC device increase with an increase in P_{inc}. This is due to the more photogenerated charge

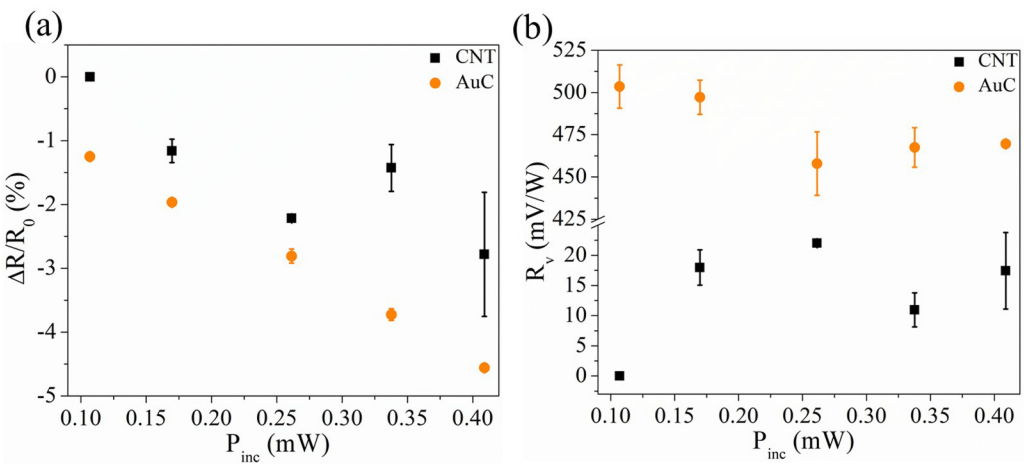

FIG. 3. Variation of (a) PR and (b) R_v with varying incident IR P_{inc}, for CNT and AuC BM, at RT.

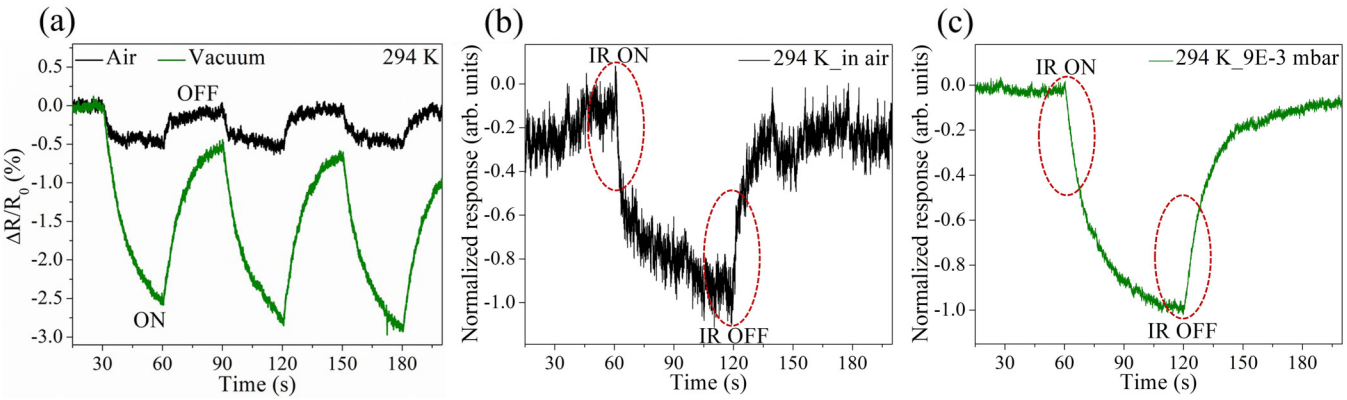

FIG. 4. (a) Temporal cyclic PR variation of AuC with IR in air and vacuum, near RT. Individually normalized IR response in (b) air and (c) in vacuum for tabulating the time taken for 50% PR change.

carriers at higher incident powers. The CNT device, on the other hand, does not show a proportionate increase for all incident powers. The tabulated R_v [Fig. 3(b)] too varies with P_{inc} with a maximum value of 503.54 ± 12.77 mV/W (bias current of 10 μA) at ∼0.11 mW P_{inc}. The as-obtained R_v under same bias current was ∼5 times the R_v reported for suspended SWCNT BM.[64] On the other hand, negative value of $\Delta R/R_0$ portrays a decrease in resistance upon IR illumination, thus suggesting photogenerated charge carriers and supporting the semiconductive behavior of the composite. A PR of ∼−1.25 ± 0.03% (for ∼0.11 mW, modulation frequency ∼1/30 s^{-1}) was observed for the AuC BM, which was ∼8.6, ∼2.5, and ∼1.3 times that of reported SWCNT BMs under unsuspended, suspended, and suspended in vacuum configurations, respectively.[64] Higher PR of AuC is due to the synergistic photothermal effect provided by the Au NPs in addition to the bolometric response of CNT to 1064 nm, i.e., NIR wavelength.[3,65–67] Upon IR illumination, the Au NPs loaded on the CNT surface increase the localized temperature (arising from photothermal effect), transferring heat to the CNT lattice and thereby resulting in an overall increased bolometric response by generating more charge carriers.

2. Effect of thermal coupling

To further establish the bolometric response of the devices, the PR was measured in air and vacuum (∼9×10^{-3} mbar) at near RT (Fig. 4). The rationale behind this measurement was to examine the effect of thermal coupling of the fabricated devices with the environment and, thus, establish the bolometric phenomenon. It is known that bolometric response decreases with the increase in thermal coupling with surroundings, and thus in accordance with this trend, the measured PR under vacuum was higher by a factor of ∼4.7 times compared to that in air [under identical

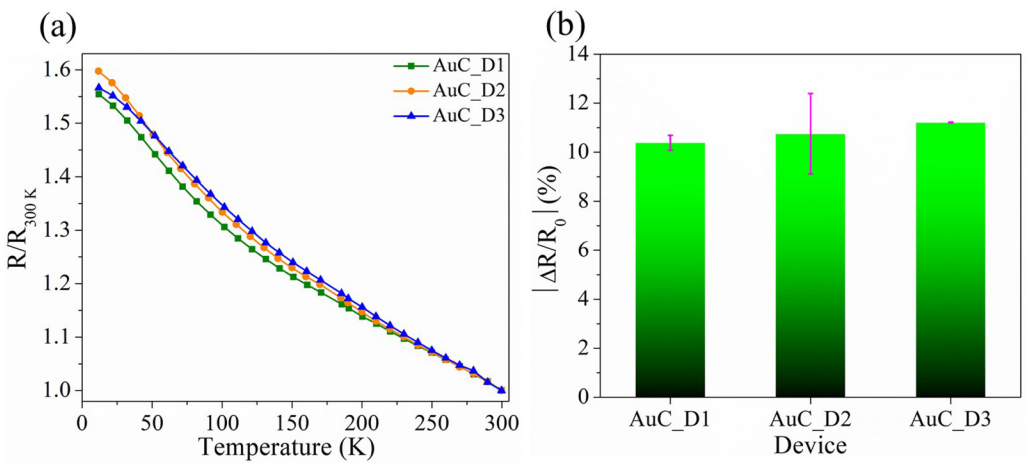

FIG. 5. (a) Variation of the normalized resistance, i.e., $R/R_{300\,K}$, with temperature and (b) PR variation at 12 K, for three identical AuC BMs under IR illumination.

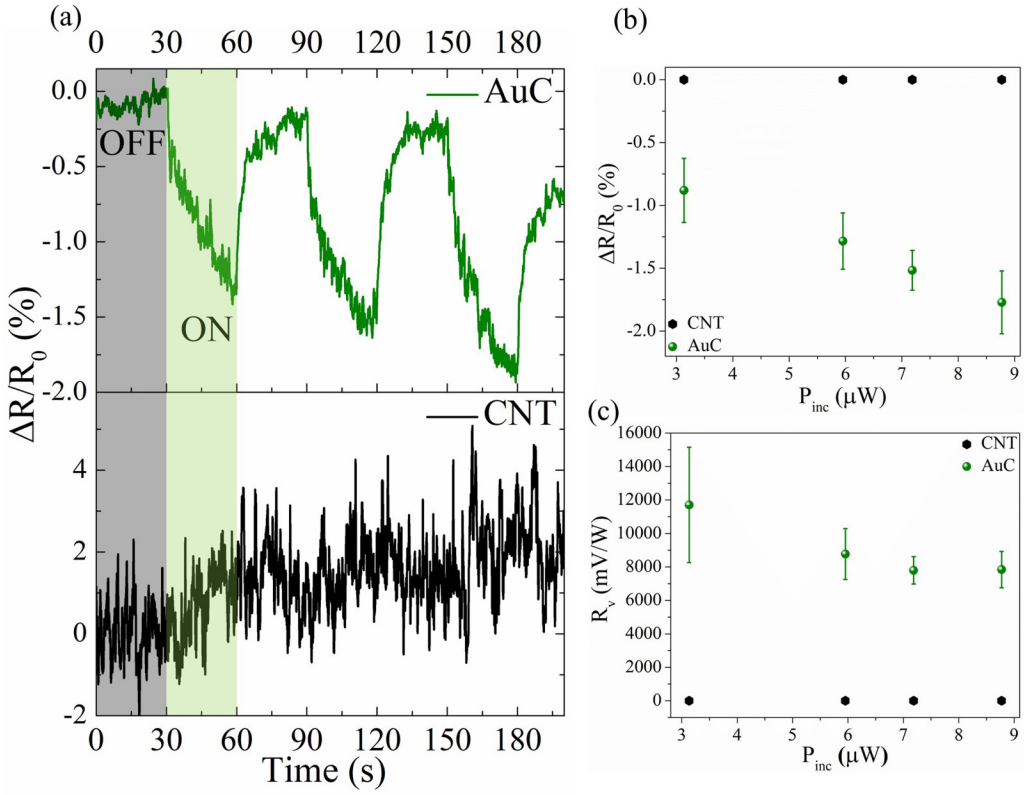

FIG. 6. (a) Temporal cyclic PR of both CNT and AuC BMs for 532 nm illumination under ambient conditions. Dependence of (b) PR and (c) R_v for varying incident powers, P_{inc}.

measurement conditions, Fig. 4(a)]. Higher PR under vacuum is a result of minimized thermal coupling with the surroundings, thus establishing the bolometric nature of the observed PR.[1,58,64,68–71]

Figures 4(b) and 4(c) represent the normalized PR in air and vacuum, respectively. Upon IR incidence in air, an abrupt change in PR from 0% to 50% was observed within a time interval of ∼3s [Fig. 4(b)], while the same being higher by a factor of ∼2.77 under vacuum [as depicted by the dashed ellipses in Figs. 4(b) and 4(c)]. Such an initial abrupt drop in PR under air is due to sudden phonon loss arising from absorbed IR heat before reaching an equilibrium state. In the case of vacuum, minimized environmental thermal coupling results in a higher thermal impedance with the environment and thereby resulting in a slow loss through other dominant sources like electrical contacts and the substrate.[58,68]

3. Performance repeatability and reproducibility

Furthermore, the device performance was verified for repeatability and reproducibility, and for this, three similar AuC BMs (AuC_D1, D2 and D3) were characterized for their bolometric performance under identical conditions. Thermal characteristics of the devices are plotted in Fig. 5(a), where the normalized resistance (with respect to 300 K) is plotted against temperature.

From the plots, it is observed that all three devices follow the similar R vs T trend. Furthermore, the quantitative analysis was performed by inspecting the variation of the value at ∼12 K. The figure of merit defined for this purpose was termed as percentage (%) variation, defined as [(standard deviation/average value) × 100]. From the plot in Fig. 5(a), it is observed that the comparative % variation in $R/R_{300\,K}$ at ∼12 K for all the three BMs is ∼1.41%, and the same for the IR response (at ∼0.11 mW P_{inc}) is ∼3.84% [Fig. 5(b)]. Such inconsequential variations in the performance metrices advocate for reproducibility of the device performance.

4. Visible bolometric characteristics

Another interesting feature of the nanocomposite BM was its spectral selectivity (wavelength-selective) and sensitivity toward visible illumination. Bolometric PR of the devices was, thus, evaluated for an illumination of 532 nm wavelength (Fig. 6) with a NdYAG laser, with measurements being performed under ambient conditions of temperature and pressure.

Figure 6(a) depicts the temporal cyclic PR comparison of CNT and AuC devices for an incident power of ∼7.2 μW. Under visible illumination, no PR was observed for the CNT BM, while the AuC BM exhibited an extraordinary PR of $\sim -1.52 \pm 0.16\%$.

TABLE I. Device response comparison for CNT and AuC BM.

	Visible @~3.13 μW				Infrared @~0.11 mW		
Device @300 K	$\Delta R/R_0$ (%)	$\lvert\Delta V\rvert(\mu V)$	R_v(mV/W)	Device @300 K	$\Delta R/R_0$ (%)	$\lvert\Delta V\rvert(\mu V)$	R_v(mV/W)
CNT	0	0	0	CNT	0	0	0
AuC	−0.88 ± 0.25	36.67 ± 10.80	11 702.02 ± 3447.12	AuC	−1.25 ± 0.03	53.83 ± 1.37	503.54 ± 12.77

Additionally, a drift in PR with time [Fig. 6(a)] is observed in the cyclic response. The measurements being performed under open ambient conditions of temperature and pressure lead to such a drift, originating from the binding/desorption of atmospheric O, stimulated by the incident light.[64] Additionally, the low thermal conductivity substrate (SiO_2/Si) beneath the nanocomposite can too contribute to the residual PR by not allowing enough heat dissipation time. Furthermore, the origin of this enhanced PR is attributed to the plasmonic effect arising from the Au NPs with the PR and photovoltage increasing with the incident power [Fig. 6(b) and S5(b) in the supplementary material, respectively] due to increased contribution from the plasmonic heat.[26] Upon incidence of 532 nm on the nanocomposite, plasmonic absorption from Au NPs, attributed to the imaginary part of its permittivity [Im(ε)], lead to losses. The loss is then manifested in terms of resistive heat originating from non-radiative decay in the Au NPs. This non-radiative decay occurs via electron–electron and electron–photon interactions, ultimately transferring the heat to the CNT lattice to increase its temperature and thereby enhance the bolometric response by generating more charge carriers. As a result of such effect from Joule heating, the heat power volume density can be expressed as

$$q_p = \varepsilon_0 \omega \mathrm{Im}(\varepsilon)|E|^2, \tag{1}$$

where ε_0 is the permittivity of free space, ω is the frequency of incident light, and E is the electric field in the NS.[72] It is, thus evident from Eq. (1) that $'q_p'$ is proportional to the frequency of incident light and the square of the electric field amplitude. Equation (1) considers the current density (J) as a function of conductivity (σ) arising from the generated E field, with the relationship $J = \sigma E$.[73,74] This leads to an extraordinary heat confinement and, thus, a very high R_v of ~11.70 ± 3.45 V/W (for 532 nm wavelength) in the AuC BM, under ambient conditions of temperature and pressure [Fig. 6(c)]. It is, however, interesting to note that for a wide range of visible incident powers (~3–9 μW), the CNT BM displays a null response. The obtained R_v, on the other hand, is ~2 (for suspended SWCNT BM with 10^{-4} A bias, under IR),[64] ~3.9 (for the 100-nm-thick film of purified SWCNTs annealed in vacuum, under IR),[68] ~10.6 (for SWCNT-polymer BM, 650 nm wavelength),[75] and ~6.5–13 (for SWCNT thermopile in the wavelength range 500–1800 nm)[76] times that of the AuC BM reported in this work for 532 nm wavelength. Alternatively, compared to a very recent result, the visible R_v is ~5.85 times that of a CNT-polymer BM, with responsivity toward 808 nm wavelength.[77] Coupling Au NPs with CNTs, thus, not only demonstrated an enhanced bolometric response under ambient conditions (uncooled BM) but also yields dual spectral sensitivity and selectivity. CNT BM responded weakly to IR illumination with noise-dominated null response for visible spectra, whereas, on the other hand, AuC BM was responsive to both wavelengths with enhanced performances. A tabular comparison of device responses toward wavelength-selectiveness and enhanced response for both CNT and AuC BM under visible (532 nm) and IR (1064 nm) illumination is presented in Table I.

III. CONCLUSIONS

In conclusion, a simple rapid green synthesis technique was adopted to synthesize an Au/CNT nanocomposite for uncooled BM. Developed techniques of spray-coating and wet-transfer along with conventional microfabrication methodologies were adopted for the complete BM fabrication. Loading Au NPs on the CNT walls resulted in improved TCR along with enhanced spectral sensitivity and selectivity under uncooled conditions. Furthermore, tuning the thermal coupling of the BM with the surrounding established the bolometric nature of the observed PR. This work, thus, demonstrates an important step in understanding and controlling the uncooled bolometric performances of the metal NP/CNT nanocomposite.

SUPPLEMENTARY MATERIAL

See the supplementary material for information on additional SEM, EDS, TEM, XPS, and XRD of the studied materials, photovoltage, and the bolometer SEM.

ACKNOWLEDGMENTS

S.N. and A.M. acknowledge funding support from MHRD, MeitY, and DST Nano Mission through NNetRA. We would also like to thank Jessy Sajan for her help toward the synthesis of the Au/CNT nanocomposite.

AUTHOR DECLARATIONS

Conflict of Interest

The authors have no conflicts to disclose.

Author Contributions

Sukanta Nandi: Conceptualization (equal); Data curation (equal); Formal analysis (equal); Writing – original draft (equal); Writing – review & editing (equal). **Vinod Panwar:** Data curation (supporting). **Abha Misra:** Conceptualization (lead); Data curation (equal); Formal analysis (equal); Funding acquisition (lead); Methodology (equal); Project administration (lead); Resources (lead); Supervision

(lead); Writing – original draft (equal); Writing – review & editing (equal).

DATA AVAILABILITY

The data that support the findings of this study are available from the corresponding author upon reasonable request.

REFERENCES

[1]R. Lu, J. J. Shi, F. J. Baca, and J. Z. Wu, J. Appl. Phys. **108**, 084305 (2010).
[2]N. A. Tomlin, C. S. Yung, Z. Castleman, M. Denoual, G. Drake, N. Farber, D. Harber, K. Heuerman, G. Kopp, H. Passe, E. Richard, J. Rutkowski, J. Sprunck, M. Stephens, C. Straatsma, S. Van Dreser, I. Vayshenker, M. G. White, S. I. Woods, W. Zheng, and J. H. Lehman, AIP Adv. **10**, 055010 (2020).
[3]S. Nandi and A. Misra, ACS Appl. Mater. Interfaces **12**, 1315 (2020).
[4]G. García-Valdivieso, H. R. Navarro-Contreras, G. Vera-Reveles, F. J. González, T. J. Simmons, M. G. Hernández, M. Quintana, and J. G. Nieto Navarro, Sens. Actuators B **238**, 880 (2017).
[5]S. Nandi and A. Misra, ACS Materials Lett. **5**, 249 (2023).
[6]W. Xu, Y. Chen, H. Zhan, and J. N. Wang, Nano Lett. **16**, 946 (2016).
[7]B. Smith, K. Wepasnick, K. E. Schrote, H.-H. Cho, W. P. Ball, and D. H. Fairbrother, Langmuir **25**, 9767 (2009).
[8]L. Stobinski, B. Lesiak, L. Kövér, J. Tóth, S. Biniak, G. Trykowski, and J. Judek, J. Alloys Compd. **501**, 77 (2010).
[9]A. K. Mishra and S. Ramaprabhu, Energy Environ. Sci. **4**, 889 (2011).
[10]F.-H. Ko, C.-Y. Lee, C.-J. Ko, and T.-C. Chu, Carbon **43**, 727 (2005).
[11]J. Xiong, Z. Zheng, X. Qin, M. Li, H. Li, and X. Wang, Carbon **44**, 2701 (2006).
[12]K. M. Liew, C. H. Wong, X. Q. He, and M. J. Tan, Phys. Rev. B **71**, 075424 (2005).
[13]S. Sharma, B. P. Singh, A. S. Babal, S. Teotia, J. Jyoti, and S. R. Dhakate, J. Mater. Sci. **52**, 7503 (2017).
[14]W. Hoenlein, F. Kreupl, G. S. Duesberg, A. P. Graham, M. Liebau, R. Seidel, and E. Unger, Mater. Sci. Eng., C **23**, 663 (2003).
[15]A. P. Graham, G. S. Duesberg, R. Seidel, M. Liebau, E. Unger, F. Kreupl, and W. Hönlein, Diamond Relat. Mater. **13**, 1296 (2004).
[16]S. Nandi, R. Vijayan, and M. Chhetri, ChemRxiv (2022).
[17]M. F. L. De Volder, S. H. Tawfick, R. H. Baughman, and A. J. Hart, Science **339**(80), 535, (2013).
[18]R. Lu, G. Xu, and J. Z. Wu, Appl. Phys. Lett. **93**, 213101 (2008).
[19]S. Nandi, B. D. Boruah, and A. Misra, Sens. Actuators A **267**, 351 (2017).
[20]G. García-Valdivieso, J. J. Velázquez-Salazar, J. E. Samaniego-Benítez, H. J. Ojeda-Galván, M. J. Arellano-Jiménez, K. G. H. Martínez-Reyna, M. José-Yacamán, and H. R. Navarro-Contreras, Nanotechnology **29**, 125607 (2018).
[21]Q. Wang, Y. Wu, X. Deng, L. Xiang, K. Xu, Y. Li, and Y. Xie, Nanomaterials **12**, 495 (2022).
[22]Q. Liang, X. Xu, H. Zhou, J. Park, J. Xu, Y. Jiang, X. Cheng, and Y. Gu, Nanotechnology **30**, 235702 (2019).
[23]S. Nandi, doctoral thesis, Indian Institute of Science, Bangalore, 2020.
[24]J.-A. Huang and L.-B. Luo, Adv. Opt. Mater. **6**, 1701282 (2018).
[25]S. A. Maier, *Plasmonics Fundamentals and Applications* (Springer Science & Business Media, 2007).
[26]M. Mahjouri-Samani, Y. S. Zhou, X. N. He, W. Xiong, P. Hilger, and Y. F. Lu, Nanotechnology **24**, 035502 (2013).
[27]H. Huang, F. Wang, Y. Liu, S. Wang, and L.-M. Peng, ACS Appl. Mater. Interfaces **9**, 12743 (2017).
[28]H. Huang, D. Zhang, N. Wei, S. Wang, and L.-M. Peng, Adv. Opt. Mater. **5**, 1600865 (2017).
[29]H. Yu, Y. Peng, Y. Yang, and Z.-Y. Li, npj Comput. Mater. **5**, 45 (2019).
[30]Z. Zanolli, R. Leghrib, A. Felten, J.-J. Pireaux, E. Llobet, and J.-C. Charlier, ACS Nano **5**, 4592 (2011).
[31]F. Li, Z. Wang, C. Shan, J. Song, D. Han, and L. Niu, Biosens. Bioelectron. **24**, 1765 (2009).
[32]T. Makaryan, S. Esconjauregui, M. Gonçalves, J. Yang, H. Sugime, D. Nille, P. R. Renganathan, P. Goldberg-Oppenheimer, and J. Robertson, ACS Appl. Mater. Interfaces **6**, 5344 (2014).
[33]M. Li, S. K. Cushing, and N. Wu, Analyst **140**, 386 (2015).
[34]C. Zhou, S. Wang, J. Sun, N. Wei, L. Yang, Z. Zhang, J. Liao, and L.-M. Peng, Appl. Phys. Lett. **102**, 103102 (2013).
[35]Y. Salamin, P. Ma, B. Baeuerle, A. Emboras, Y. Fedoryshyn, W. Heni, B. Cheng, A. Josten, and J. Leuthold, ACS Photonics **5**, 3291 (2018).
[36]A. Dorodnyy, Y. Salamin, P. Ma, J. V. Plestina, N. Lassaline, D. Mikulik, P. Romero-gomez, A. Fontcuberta i Morral, and J. Leuthold, IEEE J. Sel. Top. Quantum Electron. **24**, 1 (2018).
[37]A. Ahmadivand, M. Karabiyik, and N. Pala, *6. Plasmonic Photodetectors* (Elsevier Ltd, 2016).
[38]H. A. Atwater and A. Polman, Nature Mater **9**, 205 (2010).
[39]S. Ghods and A. Esfandiar, Nanotechnology **32**, 325203 (2021).
[40]G. V. Naik, V. M. Shalaev, and A. Boltasseva, Adv. Mater. **25**, 3264 (2013).
[41]D. Paria, V. Vadakkumbatt, P. Ravindra, S. Avasthi, and A. Ghosh, Nanotechnology **32**, 315202 (2021).
[42]P. R. West, S. Ishii, G. V. Naik, N. K. Emani, V. M. Shalaev, and A. Boltasseva, Laser Photonics Rev. **4**, 795 (2010).
[43]J. Liu, H. He, D. Xiao, S. Yin, W. Ji, S. Jiang, D. Luo, B. Wang, and Y. Liu, Materials **11**, 1833 (2018).
[44]K. L. Kelly, E. Coronado, L. L. Zhao, and G. C. Schatz, J. Phys. Chem. B **107**, 668 (2003).
[45]J. Liu, W. He, L. Hu, Z. Liu, H. Zhou, X. Wu, and L. Sun, J. Appl. Phys. **107**, 094311 (2010).
[46]D. Philip, Spectrochim. Acta Part A **77**, 807 (2010).
[47]H. Sharma, D. C. Agarwal, A. K. Shukla, D. K. Avasthi, and V. D. Vankar, J. Raman Spectrosc. **44**, 12 (2013).
[48]E. F. Antunes, A. O. Lobo, E. J. Corat, and V. J. Trava-Airoldi, Carbon **45**, 913 (2007).
[49]T. Ghodselahi, N. Aghababaie, H. Mobasheri, K. Zand Salimi, M. Akbarzadeh Pasha, and M. A. Vesaghi, Appl. Surf. Sci. **355**, 1175 (2015).
[50]A. T. E. Vilian, V. Veeramani, S.-M. Chen, R. Madhu, C. H. Kwak, Y. S. Huh, and Y.-K. Han, Sci. Rep. **5**, 18390 (2015).
[51]V. Datsyuk, M. Kalyva, K. Papagelis, J. Parthenios, D. Tasis, A. Siokou, I. Kallitsis, and C. Galiotis, Carbon **46**, 833 (2008).
[52]Q. Zehua and W. Guojian, J. Nanosci. Nanotechnol. **12**, 105 (2012).
[53]R. Atchudan, A. Pandurangan, and J. Joo, J. Nanosci. Nanotechnol. **15**, 4255 (2015).
[54]G. H. Jeong, Y. W. Lee, M. Kim, and S. W. Han, J. Colloid Interface Sci. **329**, 97 (2009).
[55]S. Krishnamurthy, A. Esterle, N.C. Sharma, and S.V. Sahi, Nanoscale Res. Lett. **9**, 627 (2014).
[56]R. Kumar, M. A. Khan, A. V. Anupama, S. B. Krupanidhi, and B. Sahoo, Appl. Surf. Sci. **538**, 148187 (2021).
[57]D. Jung, M. Han, and G. S. Lee, J. Vac. Sci. Technol. B **32**, 04E107 (2014).
[58]J. John, M. Muthee, M. Yogeesh, S. K. Yngvesson, and K. R. Carter, Adv. Opt. Mater. **2**, 581 (2014).
[59]R. Lu, C. Christianson, B. Weintrub, and J. Z. Wu, ACS Appl. Mater. Interfaces **5**, 11703 (2013).
[60]Y. Seol, A. E. Carpenter, and T. T. Perkins, Opt. Lett. **31**, 2429 (2006).
[61]V. Amendola, R. Pilot, M. Frasconi, O. M. Maragò, and M. A. Iatì, J. Phys.: Condens. Matter **29**, 203002 (2017).
[62]B. Khlebtsov, V. Zharov, A. Melnikov, V. Tuchin, and N. Khlebtsov, Nanotechnology **17**, 5167 (2006).
[63]S. Zhu, T. P. Chen, Y. C. Liu, S. F. Yu, and Y. Liu, Electrochem. Solid-State Lett. **13**, K96 (2010).

[64]R. Lu, Z. Li, G. Xu, and J. Z. Wu, Appl. Phys. Lett. **94**, 163110 (2009).
[65]Y.-C. Chuang, H.-L. Lee, J.-F. Chiou, and L.-W. Lo, J. Nanotheranostics **3**, 117 (2022).
[66]S. N. Mohammed, A. M. Mohammed, and K. F. Al-Rawi, Steroids **186**, 109091 (2022).
[67]L. Meng, W. Xia, L. Liu, L. Niu, and Q. Lu, ACS Appl. Mater. Interfaces **6**, 4989 (2014).
[68]M. E. Itkis, F. Borondics, A. Yu, and R. C. Haddon, Science **312**, 413 (2006).
[69]H. Ma, L. Pan, Q. Zhao, and W. Peng, Nanoscale **5**, 1153 (2013).
[70]L. Xiao, Y. Zhang, Y. Wang, K. Liu, Z. Wang, T. Li, Z. Jiang, J. Shi, L. Liu, Q. Li, Y. Zhao, Z. Feng, S. Fan, and K. Jiang, Nanotechnology **22**, 025502 (2011).
[71]D. Jung, M. Han, and G. S. Lee, J. Vac. Sci. Technol. B **32**, 04E105 (2014).
[72]J. Wu and Y. Wang, "Optical absorption and thermal effects of plasmonic nanostructures," in *Nanoplasmonics Fundamentals and Applications* (Rijeka InTech, 2017), p. 155.
[73]L. Jauffred, A. Samadi, H. Klingberg, P. M. Bendix, and L. B. Oddershede, Chem. Rev. **119**, 8087 (2019).
[74]S. Yushanov, J. S. Crompton, and K. C. Koppenhoefer, in *Proceedings of the COMSOL Conference* (Boston, 2013).
[75]W. Riedel, G. E. Fernandes, J. H. Kim, and J. Xu, in *SENSORDEVICES 2012, The Third Int. Conf. on Sensor Device Technologies and Applications* (Rome, 2012).
[76]B. C. St-Antoine, D. Ménard, and R. Martel, Nano Lett. **11**, 609 (2011).
[77]H. I. Murad, M. A. Mohammed, A. B. Taha, and R. K. Jamal, "Bolometric properties of uncooled semiconductor carbon nanotubes," J. Opt. (to be published).